Article:

Lee, AL orcid.org/0000-0003-0067-9183, Torvela, T orcid.org/0000-0003-1539-8755, Lloyd, GE orcid.org/0000-0002-7859-2486 et al. (1 more author) (2018) Melt organisation and strain partitioning in the lower crust. Journal of Structural Geology, 113. pp. 188-199. ISSN 0191-8141

https://doi.org/10.1016/j.jsg.2018.05.016

Melt organisation and strain partitioning in the lower crust

Amicia L. Lee, Taija Torvela, Geoffrey E. Lloyd, Andrew M. Walker

School of Earth and Environment,
University of Leeds, Leeds, LS2 9JT, UK.

Abstract

Partial melts can form as a result of crustal thickening due to orogenesis. Even small melt fractions weaken the crust, so that partially molten volumes should accumulate significant amounts of strain. However, relatively little is known of how strain partitions in partial melts, and how effective the melt expulsion processes from the partially molten crust are. Using examples from the Western Gneiss Region (WGR), Norway, we consider a case of co-existing migmatites and shear zones. Field, image analysis, and microanalytical methods allow (semi)quantification of melt volume, rock mineralogy and mineral chemistry, and microstructures. Integration of these analyses implies effective syn-melt strain partitioning and subsequent freezing of both the shear zone and migmatite texture. We propose a mechanism that allows i) syn-melt strain localisation at an outcrop scale through stress-driven melt organisation, resulting in significant relative competence differences in a partially molten rock volume; and ii) formation of fine-grained rocks at outcrop

Email addresses: `earall@leeds.ac.uk` (Amicia L. Lee), `T.M.Torvela@leeds.ac.uk` (Taija Torvela), `G.E.Lloyd@leeds.ac.uk` (Geoffrey E. Lloyd), `A.Walker@leeds.ac.uk` (Andrew M. Walker)

that is entirely or mostly syn-melt, without subsequent mylonitic shearing in the solid-state. Syn-melt shear zones that have not acted as effective melt transport channels and/or that have not accumulated post-melt deformation may be more common than conventionally assumed.

Keywords: Melt, Migmatite, Shear zone, Microstructures, Strain, Western Gneiss Region

1. Introduction

In-situ partial melting is known to cause potentially dramatic strength decreases in the crust, even for small melt volumes, constraining styles of orogenic deformation and exhumation (e.g. Beaumont et al., 2001; Rosenberg and Handy, 2005; Jamieson and Beaumont, 2013; Levine et al., 2013). Such partial melting adds to the already heterogeneous nature of most rocks (e.g. based on grain size, mineralogy, microstructure, etc.). Lithological heterogeneities are significant factors in controlling strain partitioning on all scales (Fossen and Cavalcante, 2017). However, relatively little is known about how strain partitions in partially molten rock volumes. For example, the co-existence of partially molten rock together with regions of high strain (i.e. shear zones) is a common feature of many orogenic belts (e.g. the Himalaya) but the mechanism(s) and relative timing(s) of their formation remain poorly understood.

There are known theoretical feedback relationships between melting, rheological weakening (depending on melt fraction and melt connectivity), shear zone nucleation, and melt transport so that syn-melt shear zones are expected to function as effective transport channels for crustal partial melts (e.g. Brown and Solar, 1998; Rosenberg and Handy, 2005; Brown, 2007, and references therein). Mid- and lower crustal partial melts are indeed seen to infiltrate many shear zones and source many large intrusive bodies, with some areas even showing possible direct evidence of melt removal (e.g. Brown, 1994; Johannes et al., 2003; Stuart et al., 2016).

Despite the basic relationships being known, the behaviour of partially molten crust as observed at outcrop is not always easily explained by the models and experiments (Lee et al., 2017; Rosenberg and Handy, 2005), meaning that many aspects of how partially molten crust actually deforms remain unknown. For example, it is unclear why very large volumes of melts are seen to remain approximately in-situ within the crust in the form of migmatites, despite their sometimes immediate proximity to one or several shear zones (e.g. Labrousse et al., 2004). Conversely, it remains unclear in many cases what caused the strain partitioning into a shear zone within the partially molten volume in the first place. Non-expulsion of melts might be explained by the shear zones forming post-crystallization (post-melt), but this contradicts with the theoretical predictions of inevitable formation of syn-melt shear zones (e.g. Holtzman et al., 2003; Walte et al., 2005). Another option is that the shear zones formed syn-melt but did not act as effective melt transport channels. If this is true, there may be significant implications to how partially molten crust deforms at a large scale.

In order to begin investigating the possibility of non-expulsion of partial melts through shear zones, we first need to demonstrate that such shear zones may exist. In this paper, we address this using representative rock samples from an extensively migmatized crust of the Western Gneiss Region (WGR), Norway. We use image analysis, optical microscope, Electron Backscatter Diffraction (EBSD) and electron microprobe to i) quantify leucosome fraction, ii) semi-quantify melt fraction, iii) quantify mineral geochemistry, and iv) quantify crystallographic preferred orientation (CPO) in representative rock samples from the WGR. We demonstrate that extensive partial melting and syn-melt deformation of a geochemically relatively homogeneous granitoid protolith resulted in strong strain partitioning into a syn-melt fine-grained shear zone with no melt expulsion, and no or very little post-crystallization plastic deformation.

2. Geological setting

The WGR is the deepest structural level of the Scandinavian Caledonides (Figure 1a; Andreasson and Lagerblad, 1980). It is dominated by tonalites of 1686 to 1650 Ma, subsequently intruded by granite, gabbro and diabase from 1640 to 900 Ma (Tucker et al., 1990). At 950 Ma, the igneous basement underwent granulite facies metamorphism at 900°C and 1 GPa associated with extensive plutonism (Tucker et al., 1990; Krabbendam et al., 2000; Corfu and Andersen, 2002).

Insert Figure 1

During the early Palaeozoic (480-430 Ma), the Caledonian Orogeny initiated, causing deformation and metamorphism of the Proterozoic basement gneiss and oceanic allochthons to 725°C and 1.2 GPa (Hacker et al., 2010). The final stage of the Caledonian Orogeny, the Scandian, resulted in the closure of the Iapetus Ocean and emplacement of oceanic allochthons onto Baltica between 430 and 410 Ma (Tucker et al., 2004; Hacker and Gans, 2005). Later collision of Baltica and Laurentia between 425 and 400 Ma resulted in the westward subduction of the Proterozoic Baltican basement and portions of the allochthon to ultrahigh-pressures (UHP) of 1.8-3.6 GPa and temperatures of 600-800°C (Figure 2; Andersen et al., 1991; Schärer and Labrousse, 2003; Tucker et al., 2004; Hacker and Gans, 2005; Kylander-Clark et al., 2008; Hacker et al., 2010).

From 400 to 385 Ma the WGR was exhumed to shallow crustal levels (Andersen, 1998; Terry et al., 2000; Tucker et al., 2004; Hacker, 2007; Walsh et al., 2007; Hacker et al., 2010). During the exhumation event, an E-W horizontal stretching was imprinted alongside in-situ partial melting of the gneiss via post-UHP decompression-related retrograde amphibolite metamorphism as the pressure decreased from 2.8 to 0.5 GPa at temperatures of 600 to 800^{o}C (Figure 2; Krogh, 1980; Chauvet et al., 1992; Andersen, 1998; Straume and Austrheim, 1999; Hacker et al., 2003; Labrousse et al., 2002; Schärer and Labrousse, 2003; Labrousse et al., 2004; Walsh and Hacker, 2004; Root et al., 2005; Engvik et al., 2007; Gordon et al., 2013, 2016). Evidence for (U)HP metamorphism was almost completely overprinted during the open-system partial melting event, as the UHP rocks were exhumed from 100 km depth to 15-20 km (Schärer and Labrousse, 2003; Root et al., 2005). Exhumation occurred from 394 to 389 Ma at a rate of 5 mm/year, followed by rapid cooling to reach 300°C by 357 Ma (Schärer and Labrousse, 2003; Root et al., 2005).

Insert Figure 2 (1 column figure)

This study focuses on the Nupen peninsula in the southwest of Gurskøy (Figure 1b,c). The primary lithology is amphibolite-facies quartzofeldspathic gneiss that has undergone partial melting. The gneisses show layers of melanosomes and leucosomes that were stretched and sheared at a later stage, indicating that the migmatization commenced early in the exhumation-related deformation history (Labrousse et al., 2002). Gurskøy was exhumed via thrusting and formed a NW-SE trending isoclinal fold verging southwest on the peninsula (Figure 1; Labrousse et al., 2004). Geothermometry from nearby Vanylven migmatized gneiss (approx. 5 km south of Nupen) indicate an influx of H_2O-rich fluids, allowing decompression melting to begin at 600-650°C and not exceeding 800°C (Labrousse et al., 2002, 2004; Ganzhorn et al., 2014).

Over a 1.2 km section (Figure 1c), there is a diverse deformation sequence of migmatized gneiss, mylonitic shear zones, sillimanite bearing garnet-mica schists, augen gneiss and boudinaged amphibolite dykes. The strongly deformed mylonitic shear zones extend from 5 to over 100 meters in width, but deformation is also high in the migmatitic layers, indicated by S-C fabrics and isoclinal folding of leucosome, mesosome and melanosome showing deformation is widespread over the peninsula.

Sixteen samples representing leucosome:melanosome ratio at the outcrop were taken from the different lithologies. The leucosome abundance and the degree of strain varies between different sample locations (Figure 1c).

3. Melt characteristics

In general, migmatitic melting falls into two melting reactions: granitic wet melt and dehydration melt. Granitic wet melting occurs via the simple reaction of quartz + plagioclase + K-feldspar + H_2O = melt, and begins in migmatites with a granitic protolith at approximately 650°C (Wyllie, 1977). Although the melt reaction is simple, the crystallisation products are the same as the reactants (i.e. quartz, plagioclase and K-feldspar), making identification of melt phases difficult. However, some distinctive textures may be present that are diagnostic of crystallisation from melt. These include cuspate or serrated grain boundaries with low dihedral angles (Harte et al., 1991; Sawyer, 2001; Holness and Sawyer, 2008), pseudomorphs of melt along grain boundaries and at triple/multiple junctions (Rosenberg and Riller, 2000; Holness and Sawyer, 2008), and grains with straight crystal faces that indicate crystallisation from a melt (Vernon and Collins, 1988). Dehydration melting reactions are easier to identify because of the peritectic products and melt textures. These consist of solid products of melting reactions forming euhedral crystal faces against the melt (Sawyer, 1999, 2001), reactant phases exhibiting rounded or corroded boundaries surrounded by melt films (Mehnert et al., 1973; Büsch et al., 1974), small cuspate-shaped melt pools similar to those formed in experimental studies (Harte et al., 1991; Rosenberg and Riller, 2000; Holness and Sawyer, 2008), and also inter-growths between quartz and solid products of melting (Waters, 2001; Barbey, 2007).

At the outcrop scale it is often assumed that melt is present when there is a high-temperature mineral assemblage alongside quartzofeldspathic lenses, layers or patches (i.e. the leucosome; Mehnert, 1968). However, at the microscale the leucratic material may show solid-state solution recrystallisation and deformation microstructures as opposed to melt microstructures. Here we use microstructures, image analysis and electron backscatter diffraction (EBSD) to determine melt volume and properties of a section of migmatized and sheared gneiss from the WGR where partial melting occurred during the formation of the Scandinavian Caledonides (Hacker et al., 2010, and references therein). Through analysis of textures in the migmatites and shear zones we demonstrate that even in volumes with high melt percentage, deformation may partition away from the highly molten volumes into discrete shear zones.

3.1. Macroscale evidence for melt

Nupen is comprised of migmatized gneiss, mylonitic shear zones, sillimanite bearing garnet-mica schists and augen gneiss. All lithologies have undergone varying degrees of partial melting. Figure 3 shows the characteristic outcrop scale variation across the peninsula. The migmatites are typically stromatic in structure with intense folding but have a varied leucosome content (Figure 3a,d). The next most common lithology is the mylonitic shear zones, which are strongly lineated with segregation of felsic and mafic layers (Figure 3b,c). Foliation parallel zones of garnet schist are common in the north and south (Figure 3e). The schist contains garnet porphyroblasts (0.5 to 5 cm) with the foliation defined by bands of biotite and sillimanite, hornblende, and felsics. A zone of augen gneiss is observed in the south of the Nupen peninsula; the augen (3 to 10+ cm) are mostly K-feldspar and occasionally plagioclase (Figure 3f).

Insert Figure 3

Figure 4 shows examples of the variation in the migmatized gneiss at the outcrop scale. Stromatic migmatites are most common but the leucosomes can also appear patchy, indicating the migmatite texture is surreitic or ophthalmic. Stromatic-type migmatites have the highest leucosome content (Figure 4a) and surreitic migmatites have the lowest (Figure 4c). The variation in melt fractions and migmatite structures are expected to reflect strain partitioning due to internal rheological variations.

Insert Figure 4

Macroscale leucosome content is determined via image analysis using ImageJ of digitised outcrop photos (Schneider et al., 2012). Digitising photographs and correcting for shadows or cracks on the outcrop helps to constrain leucosome vs. restite proportions. Examples of the digitised outcrop drawings are shown in figure 4. The leucosome content in the Nupen area varies from 0 to 90%. However, this does not mean up to 90% of the crust was melt, as the leucosome fraction does not necessarily equal the melt fraction. The leucosome content gives the maximum melt proportion left in-situ. It is necessary to use microstructures to distinguish if the leucosome formed from melting or solid-state deformation and recrystallisation processes.

3.2. Microstructural evidence for melt

At the microscale we are able to qualitatively determine how much of the leucosome is representative of melt and the type of migmatitic melting that occurred. The typical melt microstructures observed in the migmatites are peritectic melt products, euhedral crystal faces, cuspate-shaped melt pools, felsic compositional zoning (quartz and feldspar bands), low dihedral angles (e.g. $<60°$), disequilibrium grain boundaries, 'string of beads' texture, interstitial quartz, and myrmekite lobes (Figure 5; Sawyer, 1999, 2001; Holness et al., 2005, 2011). On their own, these microstructures would be weak indicators of melting, but when found together significantly strengthen the interpretation of melt (Vernon, 2011).

Fluid-present granitic eutectic melting starts to occur at lower temperatures (∼650°C; Wyllie, 1977) than biotite-dehydration melting (760-800°C; Spear et al., 1999). Decompression related partial melting in the WGR began at 600-650°C and did not exceed 800°C (Labrousse et al., 2002, 2004; Ganzhorn et al., 2014). Thin quartz films along grain boundaries between plagioclase and K-feldspar and occasionally biotite and K-feldspar are observed in the migmatized gneiss (Figure 5f). When the presence of quartz films is combined with the lack of garnet, the peritectic product from biotite-dehydration melting, and absence of chessboard extinction within quartz grains, they together suggest melting of the migmatites occurred at the lower end of the temperature range via granitic wet melting rather than biotite-dehydration melting. Thus, the reaction systems are:

$$\text{quartz} + \text{plagioclase} + \text{K-feldspar} + H_2O = \text{melt}, \tag{1}$$

$$\text{biotite} + \text{quartz} + \text{plagioclase} + \text{sillimanite} = \text{melt} + \text{garnet} + \text{K-feldspar}. \tag{2}$$

However the garnet schists contain both the reactants and products in Equation 2 (Figure 5i). This suggests there were different protoliths of the partially melted rocks, most likely a granitoid protolith for the migmatized gneiss and a pelitic protolith for the garnet schists (Bucher and Grapes, 2011). The abundance of biotite and presence of minor sillimanite suggests that not all the biotite and sillimanite were consumed during biotite-dehydration melting and/or the biotite and sillimanite are retrograde. Here we focus on the fluid-present granitic eutectic melting of the migmatitic gneiss to determine the melt fraction and styles from microstructures.

Insert Figure 5

If melting occurs under static conditions and absence of deformation in an igneous setting, the grains crystallised from melt will reach a textural equilibrium with a uniform grain size and grain boundary angles relative to interfacial angles (e.g. 103 to 115° for quartz, plagioclase or K-feldspar; Vernon, 1968). This does not apply to the migmatites from the WGR as partial melting occurred under a deformation regime via decompression related retrograde metamorphism. As a result we mainly observe irregular grain boundaries and low dihedral angles (<60°) as the migmatite crystallised in textural disequilibrium (Figure 5a).

Dihedral angles play a key role in melt connectivity: melt is likely to be interconnected if the melt-solid dihedral angle is less than 60°, but is likely to form isolated pockets when greater than 60° (Holness, 2006; Holness et al., 2011). Thus, if there is a high dihedral angle the melt connectivity is low and the strength of the partially melted rock would be greater than if there is a low dihedral angle where the melt connectivity is high. Figure 5b shows examples of the high and low dihedral angles observed in our samples. Following the method of Holness et al. (2005) a sample of 50 dihedral angles were measured for each thin section. Figure 6 shows results of solid-solid-melt and solid-solid-solid dihedral angles, where the relationship between median angle and standard deviation indicate melt-present or solid-state equilibrium. We observe a median dihedral angle of 53° for all boundaries, 37° for solid-solid-melt boundaries and 88° for solid-solid-solid boundaries (Figure 6). Where melt is present it is observed to be connected and thus the strength of the migmatite during melting is low.

Insert Figure 6

The 'string of beads' texture of quartz grains is also observed in some WGR samples (Figure 5a). This texture usually forms during concentration of melt from thick films on grain boundaries into 'beads' (Holness et al., 2011). The texture suggests a slow crystallisation rate to allow nucleation of individual grains from melt films (Holness et al., 2011). Interstitial melt can appear similar to the 'string of beads' texture. This is more commonly observed and may represent larger collections of crystallised melt that did not separate into individual beads. Irregular grains of quartz with lobate (Figure 5c) and cuspate (Figure 5b,d,e) grain boundaries are also commonly present. Figure 5d shows embayed biotite and plagioclase where quartz has penetrated into the non-melt grains. Fingers of inferred former melt with small dihedral angles are shown in Figure 5b and commonly align parallel to foliation. The shear zone samples also show interstitial quartz infilling pore space implying they have also melted (Figure 5e).

Lobes of myrmekite are very common in the migmatized gneisses and are also present in small amounts in the shear zone samples; however, their origin is controversial. It has been proposed that they originated either from a quenched fluid-rich melt (Hibbard, 1979, 1987) or that they represent solid-state reactions in the presence of hydrous fluid (e.g. Ashworth, 1972; Phillips, 1974, 1980; Simpson and Wintsch, 1989; Vernon, 1991; Yuguchi and Nishiyama, 2008; Vernon, 2011). Figure 5h shows a large K-feldspar grain mantled by myrmekite lobes, which may be of melt origin as they co-exist with other melt microstructures. Myrmekite is also observed in the shear zone, figure 5g shows a coarse myrmekite band as well as finer myrmekite mantling K-feldspar grains. Conversely if they are a solid-state texture, they indicate deformation occurred post-melt in a fluid-rich system.

Insert Figure 7

Insert Figure 8 (1 column figure)

To understand the effects of melt on rheology, it is important to quantify the melt fraction. Microscale melt determination is qualitative as we use microstructures indicative of melt or the former presence of melt. With the use of ImageJ we are able to isolate the melt and solid fractions of the rock. Plane polarised (PPL) and cross-polarised (XPL) light photomicrographs with and without gypsum plate are used to construct the melt-solid interpretations. Figure 7 shows examples of the quantification of the migmatized gneiss via photomicrographs and corresponding interpretations of melt (white) vs. solid (grey). Figure 8 shows the comparison between leucosome volume at the macroscale and melt volume at the microscale. In the Nupen area, the leucosome volume is more than twice the interpreted microstructural melt content, leading to a possible overestimation and an unreliable method of calculating accurate melt volumes in the field. Nevertheless the leucosome and the interpreted melt percentages are systematically higher in the migmatite gneisses outside the shear zones. The calculated melt percentage assumes all melt was liquid at the same time, which is unlikely.

4. Mineral assemblages and compositions

In the WGR we see evidence for fine grained shear zones in a migmatized gneiss, but what is the timing of melting with respect to the shear zones? To investigate how the shear zones are related to the migmatites, we use microanalytical techniques to compare the migmatites and shear zone samples. WGR12 is a migmatized gneiss with 18-20% melt in the microstructure and WGR13 is a mylonitized gneiss with ∼1% melt in the microstructure. Figure 9 shows backscattered electron maps of both samples where there is a grain size variation of 0.2 to 5 mm in the migmatite and 0.05 to 0.3 mm in the shear zone.

Insert Figure 9

If the shear zone has not undergone partial melting or was originally a different layer of rock, we would expect to see different mineralogies due to melt reactions that would have occurred in the migmatite. However, if the protolith was fairly homogeneous and the mylonite-like fabric formed via syn-melt shearing, the melt reactions will produce the same mineralogy for the migmatized and mylonitized gneisses. In detail, there may be small differences between the migmatite and shear zone as more melt loss is likely to have occurred via transport through the shear zone than in the migmatized wall rock as indicated in Figure 8.

Insert Table 1

The mineral compositions in the migmatites and shear zones are the same; quartz, K-feldspar, plagioclase, biotite and minor hornblende. The modal proportions are calculated via the number of points indexed from EBSD and shown in Table 1. Quartz is the most abundant mineral in both samples followed by K-feldspar. K-feldspar makes up more of WGR12 than WGR13 but this is due to large K-feldspar grains dominating the sample. As the modal compositions are similar it suggests there has not been a significant change in mineralogy due to melt reactions or melt loss between the two samples. Both observed leucosome and interpreted melt volume are much lower than in surrounding migmatites, mineralogical proportions suggest the leucosome is underestimated greatly in the shear zone due to the small grain size.

Spot analyses for plagioclase (plag), K-feldspar (kfs), biotite (bte) and hornblende (hbl) were measured with the University of Leeds, JEOL JXA8230 electron microprobe operated at 15kV and 15nA with a defocused beam (Table 1). The results show there are no significant variations in the major or minor elements. Plagioclase and some K-feldspar represent the melt phase and the element totals are similar between the migmatite and shear zone samples. Both samples indicate the plagioclase is andesine in composition (An_{32-48}), although some analyses indicate a more sodic composition, due to the perthitic relationship between plagioclase and K-feldspar where albite forms the perthite. Mineral compositions and abundances suggest a protolith of a granitic composition such as felsic gneiss (Bucher and Grapes, 2011). The similarities in element totals suggest the shear zone was involved in melting and did not permit increased melt loss when compared to the migmatites.

5. Crystallographic Preferred Orientations

If the shear zones have not undergone melting they should preserve a record of pre-, syn- and post-melt deformation(s). In particular, the lack of pervasive melting means the crystal microstructure has not been 'reset' in non-melt zones and hence should be observed in crystallographic preferred orientations (CPO). In contrast, if all of the gneiss is involved in melting and the shear zone forms syn-melting, any pre-existing fabric will have been 'reset' with crystallisation under the same stresses for the migmatite and shear zone. Subsequent deformation may occur but the post-melt CPO from the migmatite should be recognisable in the shear zone CPO which would be strong to reflect the deformation. We compare the CPO for the adjacent migmatite, WGR12, and shear zone, WGR13, to identify timing of deformation relative to melting.

Insert Figure 10

CPO results were measured via EBSD using a FEI Quanta 650 FEG-ESEM with AZtec software and an Oxford/HKL Nordlys S EBSD system at the University of Leeds (mapped areas are shown in Figure 9). Figure 10 shows the CPO for biotite and quartz in samples WGR12 and WGR13 (plagioclase and K-feldspar CPO is available in supporting information). The biotite represents a solid phase whereas the quartz represents one of the melt phases.

Figure 10a,b shows the biotite CPO for both samples, they are somewhat similar both exhibiting strong c-axes maxima parallel (||) to Z, although more dispersed in WGR12 (e.g. Ji et al., 2015). Similarly, single girdles parallel to basal plane for $< a >$ and $< b >$, again, less well-defined for WGR12 with distinct a-max||X and b-max||Y in WGR13. The presence of the girdles and a/b-max suggest gliding on the $< 001 >$ parallel to $< 100 >$ or perhaps $< 110 >$, which is the average of $< 100 >$ and $< 010 >$ in WGR13. However, the dispersion of a and b in a girdle parallel to XY for WGR12 plane could indicate 'floating' in a melt. The dispersed c-max is compatible with this idea as it indicates slight 'floating' induced undulation. As a result, the WGR12 biotite CPO is more likely the effect of a syn-melt fabric and controlled by the shape preferred orientation of biotite aligned by flow of the melt instead of a deformation induced CPO present in the shear zone.

The quartz CPO are generally weak for both the shear zone and especially migmatite samples (Figure 10c,d). If deformation to form the shear zone occurred pre- or post-melt producing a mylonite, we would expect to see a strong CPO in WGR13. However, the weak CPO is atypical for a mylonite (Toy et al., 2008; Barth et al., 2010) suggesting there was not much deformation in solid-state (Figure 10d). Furthermore, whilst both samples indicate r||Y as a possible vorticity axis in quartz, the biotite CPO's imply no such rotation. This suggests any deformation is preferentially irrotational (i.e. 'pure shear') for biotite whereas it is rotational (i.e. 'simple shear') for quartz. By comparison with VPSC models (Morales et al., 2014), the quartz CPO correlates with amphibolite facies r-slip simple shear simulations ($\gamma = 1.73$). This implies both melt and crystallisation occurred within the amphibolite facies (Chauvet et al., 1992; Andersen, 1998; Schärer and Labrousse, 2003; Labrousse et al., 2011). In summary, the similarities between the CPO for the migmatite, WGR12, and the shear zone, WGR13, suggest the CPO were reset during the melting event; the lack of strength in the shear zone CPO and similarities with the migmatite CPO suggests deformation was transient or even absent post-melting.

6. Discussion

Searle (2013) posed the question "do shear zones control the generation and ascent of magmas (Brown and Solar, 1998; Brown, 2007) or do magmas trigger nucleation of shear zones?". The Nupen peninsula has fine grained shear zones within migmatized gneiss. However, there is no evidence for significant mineral chemistry variations or post-crystallisation strain in the shear zone. We propose a hypothesis that grain size reduction is a result of initial syn-melt shearing which results in the observed geometry of the bodies (thin laminae/sheets of melt). The layering constrained grain growth and increased heterogeneous nucleation rates to maintain a small grain size.

Low dihedral angles, interstitial quartz infilling pore space and myrmekite are present in shear zone samples from Nupen (Figure 5e). These microstructures are not strong evidence of melting, but when taken together and considering the close proximity to the migmatites it is likely melt was present in the shear zones. If the shear zones were active post-melting, the melt microstructures are likely to have been erased by solid-state processes. Here we do not see deformation of the melt microstructures in solid-state (Figure 5e), suggesting the shear zone was active pre- or syn-melt. As well as the shear zone microstructures, the alignment of the foliation, shear zones and melt 'fingers' in the migmatite is evidence for a single pattern of strain for the formation of all three features, suggesting a syn-melt fabric.

The absence of significant variations in mineralogy or mineral chemistry between the migmatite and shear zone suggest the protolith was the same (Figure 1), most likely a felsic gneiss to allow for fluid-present granitic melting (Equation 1). This suggests melt was pervasive through the migmatite and shear zone. The shear zone may have been used as a pathway for melt loss but the mineralogy suggests no evidence for melt loss or gain in the shear zone. This suggests the shear zone was short-lived as the migmatite was not 'drained' of melt relative to the shear zone.

The strong biotite CPO is expected for the shear zone sample with strong c-axes maximum and normal to foliation in $< a >$ and $< b >$. The biotite CPO for the migmatite is similar to the CPO from the shear zone but more diffuse. The similarity between the CPO's suggests deformation occurred under the same stress field resulting in passive rotation of the biotite grains sub-perpendicular to the maximum normal stress component. Although the shear zone sample appears to have a mylonitic fabric, the quartz CPO is not typical for a mylonite (Toy et al., 2008; Barth et al., 2010). We suggest syn-melt deformation of the quartz with progressive crystallisation results in a weak CPO regardless of deformation intensity. As there is little evidence for post-melt deformation in the CPO, we suggest grain size reduction gives the appearance of a mylonite that formed syn-melt.

Insert Figure 11 (1 column figure)

As a result of the microstructural and petrology data, we propose a model for melt organisation, strain localisation and formation of a fine grain size during partial melting. The model starts with a homogeneous solid gneiss where strain is distributed evenly (Figure 11a). Melting is generally evenly distributed throughout the leucosome; however, where melt connectivity is slightly higher, the melt organises into layers whereas elsewhere it remains as disorganised 'pools' (Figure 11b,c).

The organised melt system results in a viscosity reduction compared to the disorganised melt system and in turn results in a higher strain for a lower shear stress as shown by Rosenberg and Handy (2005). Increased shearing of the melt thins the melt layers (Figure 11d). Strain localises into the melt zones resulting in a stress-driven organisation of melt (Brown and Solar, 1998; Rosenberg and Handy, 2005; Vanderhaeghe, 2009). The melt drains from the nearby migmatite into the shear zones and forms the initial stages of a melt pathway and the mylonite-like fabric. We suggest the shear zones at Nupen are short-lived and do not develop melt pathways to expel melt from the system.

The shear zones formed thin melt bands due to higher strain accommodation when the rocks were partially molten. This layering constrained grain growth and increased heterogeneous nucleation rates in the fine grained rocks. When the melt crystallised the grains do not have the space (or surface energy) to grow. This resulted in the small grain size in the organised melt layers, than the disorganised melt layers giving the mylonitic appearance seen at outcrop scale today (Figure 11e). This process induces a mylonitic macroscale appearance of the shear zone without the solid-state deformation fabric expected of a mylonite. The melt organisation process generates (or preserves) grain size heterogeneity without significant solid-state deformation in shear zones after solidification of the migmatite. This means a mechanism for later strain localisation is preserved in a system which has not undergone later deformation. The resulting heterogeneity allows formation of shear zones in areas such as South Armorcian Shear Zone, Brittany (Brown and Dallmeyer, 1996), Wet Mountains, Colorado (Levine et al., 2013), and the Himalayas and Karakoram (Searle, 2013) where there is a longer history of post solidification deformation.

7. Conclusions

In this study we have interpreted the mechanisms for strain partitioning at Nupen in the WGR, Norway. We observe a feedback process where reorganisation of the melt leads to strain localisation and grain size reduction, which in turn results in increased strain partitioning.

Whereas mylonite-like fine grained rocks are normally interpreted to have formed due to shearing in the solid-state, here we observe a mylonite-like rock that probably formed while partially molten and, therefore, lack the deformed microstructure of a mylonite. This situation implies that while partially molten volumes are weaker than completely solid rock, internal heterogeneities may result in significant differences in relative, effective rheology and therefore strain partitioning. An important implication is syn-melt shear zones do not necessarily lead to melt expulsion, here we see no evidence of increased melt loss or melt accumulation as the migmatite transitions into the shear zones.

Fine grained shear zones are not necessarily post-melt or retrograde mylonites. The once-molten rocks do not necessarily accumulate further strain once crystallised. However, the organisation of partial melt forming syn-melt shear zones could be the origin of the mechanical heterogeneity needed to allow later strain localisation. If the shear zones continued to deform post-melting in the solid-state we would expect to see strain localise into the shear zones with evidence for solid-state deformation and the loss of melt microstructures. This process would produce the mylonitic fabrics observed in shear zones.

Acknowledgements

ALL thanks the Timothy Jefferson Field Research fund, part of the Geological Society of London's 2015 research grants, which helped to fund fieldwork in Norway; Andrew Parsons is also thanked for field assistance. We thank Marian Holness, Brendan Dyck and Gautier Nicoli for advice on melt microstructures. AMW is grateful for support from the UK Natural Environment Research Council (NE/K008803/1 and NE/M000044/1). The authors thank Nicolas Walte and Scott Paterson for their helpful reviews and editor Bill Dunn for valuable comments.

References

Andersen, T. B., 1998. Extensional tectonics in the Caledonides of southern Norway, an overview. Tectonophysics 285 (3-4), 333–351.

Andersen, T. B., Jamtveit, B., Dewey, J. F., Swensson, E., 1991. Subduction and eduction of continental crust: major mechanisms during continentcontinent collision and orogenic extensional collapse, a model based on the south Norwegian Caledonides. Terra Nova 3 (3), 303–310.

Andreasson, P. G., Lagerblad, B., 1980. Occurrence and significance of inverted metamorphic gradients in the western Scandinavian Caledonides. Journal of the Geological Society 137 (3), 219–230.

Ashworth, J. R., 1972. Myrmekites of exsolution and replacement origins. Geological Magazine 109 (1), 45–62.

Ashworth, J. R. (Ed.), 1985. Migmatites. Blackie, Glasgow.

Auzanneau, E., Vielzeuf, D., Schmidt, M. W., 2006. Experimental evidence of decompression melting during exhumation of subducted continental crust. Contributions to Mineralogy and Petrology 152 (2), 125–148.

Barbey, P., 2007. Diffusion-controlled biotite breakdown reaction textures at the solid/ liquid transition in the continental crust. Contributions to Mineralogy and Petrology 154 (6), 707–716.

Barth, N. C., Hacker, B. R., Seward, G. G. E., Walsh, E. O., Young, D., Johnston, S., 2010. Strain within the ultrahigh-pressure Western Gneiss region of Norway recorded by quartz CPOs. Geological Society, London, Special Publications 335, 663–685.

Beaumont, C., Jamieson, R. A., Nguyen, M. H., Lee, B., 2001. Himalayan tectonics explained by extrusion of a low-viscosity crustal channel coupled to focused surface denudation. Nature 414 (December), 738–742.

Brown, M., 1994. The generation, segregation, ascent and emplacement of granite magma: the migmatite-to-crustally-derived granite connection in thickened orogens. Earth Science Reviews 36 (1-2), 83–130.

Brown, M., 2007. Old Crustal melting and melt extraction, ascent and emplacement in orogens: mechanisms and consequences. Journal of the Geological Society 164 (4), 709–730.

Brown, M., Dallmeyer, R. D., may 1996. Rapid Variscan exhumation and the role of magma in core complex formation: southern Brittany metamorphic belt, France. Journal of Metamorphic Geology 14 (3), 361–379.

Brown, M., Solar, G. S., 1998. Granite ascent and emplacement during contractional deformation in convergent orogens. Journal of Structural Geology 20 (9-10), 1365–1393.

Bucher, K., Grapes, R., 2011. Metamorphic Rocks. In: Petrogenesis of Metamorphic Rocks. Springer-Verlag, Berlin, Ch. 2, pp. 21–56.

Büsch, W., Schneider, G., Mehnert, K. R., 1974. Initial melting at grain boundaries. Part II: melting in rocks of granodioritic, quartzdioritic and tonalitic composition. Neues Jahrbuch für Mineralogie, Monatshefte 8, 345–370.

Carswell, D. A., Brueckner, H. K., Cuthbert, S. J., Mehta, K., Brien, P. J. O., 2003. The timing of stabilisation and the exhumation rate for ultra-high pressure rocks in the Western Gneiss Region of Norway. Journal of Metamorphic Geology 21 (6), 601–612.

Chauvet, A., Kienast, J. R., Pinardon, J. L., Brunel, M., 1992. Petrological Constraints and Pt Path of Devonian Collapse Tectonics within the Scandian Mountain Belt (Western Gneiss Region, Norway). Journal of the Geological Society 149, 383–400.

Corfu, F., Andersen, T. B., 2002. U-Pb ages of the Dalsfjord complex, SW Norway, and their bearing on the correlation of allochthonous crystalline segments of the Scandinavian Caledonides. International Journal of Earth Sciences 91 (6), 955–963.

Engvik, A. K., Andersen, T. B., Wachmann, M., 2007. Inhomogeneous deformation in deeply buried continental crust, an example from the eclogite-facies province of the Western Gneiss Region, Norway. Norsk Geologisk Tidsskrift 87 (4), 373–389.

Fossen, H., Cavalcante, G. C. G., 2017. Shear zones A review. Earth-Science Reviews 171 (May), 434–455.

Ganzhorn, A. C., Labrousse, L., Prouteau, G., Leroy, C., Vrijmoed, J. C., Andersen, T. B., Arbaret, L., aug 2014. Structural, petrological and chemical analysis of syn-kinematic migmatites: insights from the Western Gneiss Region, Norway. Journal of Metamorphic Geology 32 (6), 647–673.

Gordon, S. M., Whitney, D. L., Teyssier, C., Fossen, H., 2013. U-Pb dates and trace-element geochemistry of zircon from migmatite, Western Gneiss Region, Norway: Significance for history of partial melting in continental subduction. Lithos 170-171, 35–53.

Gordon, S. M., Whitney, D. L., Teyssier, C., Fossen, H., Kylander-Clark, A. R. C., 2016. Geochronology and geochemistry of zircon from the northern Western Gneiss Region: Insights into the Caledonian tectonic history of western Norway. Lithos 246-247, 134–148.

Hacker, B. R., 2007. Ascent of the ultrahigh-pressure Western Gneiss Region , Norway. Geological Society of America, Special Papers 419, 171–184.

Hacker, B. R., Andersen, T. B., Johnston, S., Kylander-Clark, A. R. C., Peterman, E. M., Walsh, E. O., Young, D., 2010. High-temperature deformation during continental-margin subduction & exhumation: The ultrahigh-pressure Western Gneiss Region of Norway. Tectonophysics 480 (1-4), 149–171.

Hacker, B. R., Andersen, T. B., Root, D. B., Mehl, L., Mattinson, J. M., Wooden, J. L., 2003. Exhumation of high-pressure rocks beneath the Solund Basin, Western Gneiss Region of Norway. Journal of Metamorphic Geology 21 (6), 613–629.

Hacker, B. R., Gans, P. B., 2005. Continental collisions and the creation of ultrahigh-pressure terranes: Petrology and thermochronology of nappes in the central Scandinavian Caledonides. Bulletin of the Geological Society of America 117 (1-2), 117–134.

Harte, B., Pattison, D. R. M., Linklater, C. M., 1991. Field relations and petrography of partially melted pelitic and semi-pelitic rocks. In: Equilibrium and Kinetics in Contact Metamorphism: the Ballachulish Igneous Complex and its Aureole. Springer, Heidelberg, pp. 181–210.

Hibbard, M. J., 1979. Myrmekite as a marker between preaqueous and postaqueous phase saturation in granitic systems. Geological Society of America Bulletin 90 (11), 1047–1062.

Hibbard, M. J., 1987. Deformation of incompletely crystallized magma systems: granitic gneisses and their tectonic implications. Journal of Geology 95 (4), 543–561.

Holness, M. B., 2006. Melt-solid dihedral angles of common minerals in natural rocks. Journal of Petrology 47 (4), 791–800.

Holness, M. B., Cesare, B., Sawyer, E. W., 2011. Melted rocks under the microscope: Microstructures and their interpretation. Elements 7 (4), 247–252.

Holness, M. B., Cheadle, M. J., McKenzie, D. P., 2005. On the use of changes in dihedral angle to decode late-stage textural evolution in cumulates. Journal of Petrology 46 (8), 1565–1583.

Holness, M. B., Sawyer, E. W., 2008. On the pseudomorphing of melt-filled pores during the crystallization of migmatites. Journal of Petrology 49 (7), 1343–1363.

Holtzman, B. K., Groebner, N. J., Zimmerman, M. E., Ginsberg, S. B., Kohlstedt, D. L., 2003. Stress-driven melt segregation in partially molten rocks. Geochemistry, Geophysics, Geosystems 4 (5), 1–26.

Jamieson, R. A., Beaumont, C., 2013. On the origin of orogens. Bulletin of the Geological Society of America 125 (11), 1671–1702.

Ji, S., Shao, T., Michibayashi, K., Oya, S., Satsukawa, T., Wang, Q., Zhao, W., Salisbury, M. H., 2015. Magnitude and symmetry of seismic anisotropy in mica-and amphibole-bearing metamorphic rocksand implications for tectonic interpretationof seismic data from the southeastTibetan Plateau. Journal of Geophysical Research: Solid Earth 160 (9), 6404–6430.

Johannes, W., Ehlers, C., Kriegsman, L. M., Mengel, K., jun 2003. The link between migmatites and S-type granites in the Turku area, southern Finland. Lithos 68 (3-4), 69–90.

Kildal, E. S., 1970. Geologisk kart over Noreg Måløy: Trondheim. Norges Geologiske Undersøking scale 1:25.

Krabbendam, M., Wain, A., Andersen, T. B., 2000. Pre-Caledonian granulite and gabbro enclaves in the Western Gneiss Region, Norway: indications of incomplete transition at high pressure. Geological Magazine 137 (3), 235–255.

Krogh, E. J., 1980. Geochemistry and petrology of glaucophane-bearing eclogites and associated rocks from Sunnfjord, Western Norway. Lithos 13 (4), 355–380.

Kylander-Clark, A. R. C., Hacker, B. R., Mattinson, J. M., 2008. Slow exhumation of UHP terranes: Titanite and rutile ages of the Western Gneiss Region, Norway. Earth and Planetary Science Letters 272 (3-4), 531–540.

Labrousse, L., Jolivet, L., Agard, P., Hebert, R., Andersen, T. B., aug 2002. Crustal-scale boudinage and migmatization of gneiss during their exhumation in the UHP Province of Western Norway. Terra Nova 14 (4), 263–270.

Labrousse, L., Jolivet, L., Andersen, T. B., Agard, P., Maluski, H., 2004. Pressure-temperature-time deformation history of the exhumation of ultra-high pressure rocks in the Western Gneiss Region, Norway. Geological Society of America, Special Papers 380, 155–183.

Labrousse, L., Prouteau, G., Ganzhorn, A. C., 2011. Continental exhumation triggered by partial melting at ultrahigh pressure. Geology 39 (12), 1171–1174.

Lee, A. L., Walker, A. M., Lloyd, G. E., Torvela, T., 2017. Modeling the impact of melt on seismic properties during mountain building. Geochemistry, Geophysics, Geosystems 18 (3), 1090–1110.

Levine, J. S. F., Mosher, S., Siddoway, C. S., 2013. Relationship between syndeformational partial melting and crustal-scale magmatism and tectonism across the Wet Mountains, central Colorado. Lithosphere 5 (5), 456–476.

Lutro, O., Robinson, P., Solli, A., 1997. Proterozoic geology and Scandian overprinting in the Western Gneiss Region. Norges Geologiske Undersøkelse 97, 86.

Lutro, O., Tveten, E., 1998. Geologisk kart over Noreg Årdal: Trondheim. Norges Geologiske Undersøking scale 1:25.

Mehnert, K. R., 1968. Migmatites and the origin of granitic rocks. Elsevier, Amsterdam.

Mehnert, K. R., Büsch, W., Schneider, G., 1973. Initial melting at grain boundaries of quartz and feldspar in gneisses and granulites. Neues Jahrbuch für Mineralogie, Monatshefte 4, 165–183.

Morales, L. F., Lloyd, G. E., Mainprice, D., 2014. Fabric transitions in quartz via viscoplastic self-consistent modeling part I: Axial compression and simple shear under constant strain. Tectonophysics 636, 52–69.

Phillips, E. R., 1974. Myrmekite - one hundred years later. Lithos 7 (3), 181–194.

Phillips, E. R., 1980. On polygenetic myrmekite. Geological Magazine 117 (1), 29–36.

Root, D. B., Hacker, B. R., Gans, P. B., Ducea, M. N., Eide, E. A., Mosenfelder, J. L., 2005. Discrete ultrahigh-pressure domains in the Western Gneiss Region, Norway: Implications for formation and exhumation. Journal of Metamorphic Geology 23 (1), 45–61.

Rosenberg, C. L., Handy, M. R., 2005. Experimental deformation of partially melted granite revisited: implications for the continental crust. Journal of Metamorphic Geology 23 (1), 19–28.

Rosenberg, C. L., Riller, U., 2000. Partial-melt topology in statically and dynamically recrystallized granite. Geology 28 (1), 7–10.

Sawyer, E. W., 1999. Criteria for the Recognition of Partial Melting. Physics and Chemistry of the Earth, Part A: Solid Earth and Geodesy 24 (3), 269–279.

Sawyer, E. W., may 2001. Melt segregation in the continental crust: distribution and movement of melt in anatectic rocks. Journal of Metamorphic Geology 19 (3), 291–309.

Schärer, U., Labrousse, L., 2003. Dating the exhumation of UHP rocks and associated crustal melting in the Norwegian Caledonides. Contributions to Mineralogy and Petrology 144 (6), 758–770.

Schneider, C. A., Rasband, W. S., Eliceiri, K. W., 2012. NIH Image to ImageJ: 25 years of image analysis. Nature Methods 9 (7), 671–675.

Searle, M., 2013. Crustal melting, ductile flow, and deformation in mountain belts: Cause and effect relationships. Lithosphere 5 (6), 547–554.

Simpson, C., Wintsch, R. P., 1989. Evidence for deformation-induced K-feldspar replacement by myrmekite. Journal of Metamorphic Geology 7 (2), 261–275.

Spear, F. S., Kohn, M. J., Cheney, J. T., 1999. P -T paths from anatectic pelites. Contributions to Mineralogy and Petrology 134, 17–32.

Straume, Å. K., Austrheim, H., 1999. Importance of fracturing during retro-metamorphism of eclogites. Journal of Metamorphic Geology 17 (6), 637–652.

Stuart, C. A., Piazolo, S., Daczko, N. R., 2016. Mass transfer in the lower crust: Evidence for incipient meltassisted flow along grain boundaries in the deep arc granulitesof Fiordland, New Zealand. Geochemistry, Geophysics, Geosystems 17, 3733–3753.

Terry, M. P., Robinson, P., Hamilton, A., Jercinovic, M. J., 2000. Monazite geochronology of UHP and HP metamorphism, deformation, and exhumation, Nordøyane, Western Gneiss Region, Norway. American Mineralogist 85 (11-12), 1651–1664.

Toy, V. G., Prior, D. J., Norris, R. J., 2008. Quartz fabrics in the Alpine Fault mylonites: Influence of pre-existing preferred orientations on fabric development during progressive uplift. Journal of Structural Geology 30 (5), 602–621.

Tucker, R. D., Krogh, T. E., Råheim, A., 1990. Proterozoic evolution and age-province boundaries in the central part of the Western Gneiss Region, Norway: Results of U-Pb dating of accessory minerals from Trondheimsfjord to Geiranger. Mid-Proterozoic Laurentia-Baltica 38, 149–173.

Tucker, R. D., Robinson, P., Solli, A., Gee, D. G., Thorsnes, T., Krogh, T. E., Nordgulen, Ø., Bickford, M. E., 2004. Thrusting and extension in the Scandian Hinterland, Norway: New U-Pb ages and tectonostratigraphic evidence. American Journal of Science 304 (6), 477–532.

Tveten, E., Lutro, O., Thorsnes, T., 1998. Geologisk kart over Noreg Ulsteinvik: Trondheim. Norges Geologiske Undersøkelse scale 1:25.

Vanderhaeghe, O., nov 2009. Migmatites, granites and orogeny: Flow modes of partially-molten rocks and magmas associated with melt/solid segregation in orogenic belts. Tectonophysics 477 (3-4), 119–134.

Vernon, R. H., 1968. Microstructures of high-grade metamorpbic rocks at broken hill, Australia. Journal of Petrology 9 (1), 1–22.

Vernon, R. H., 1991. Questions about myrmekite in deformed rocks. Journal of Structural Geology 13 (9), 979–985.

Vernon, R. H., 2011. Microstructures of melt-bearing regional metamorphic rocks. GSA Memoirs 207 (01), 1–11.

Vernon, R. H., Collins, W. J., 1988. Igneous microstructures in migmatites. Geology 16 (January 2009), 1126–1129.

Walsh, E. O., Hacker, B. R., 2004. The fate of subducted continental margins: Two-stage exhumation of the high-pressure to ultrahigh-pressure Western Gneiss Region, Norway. Journal of Metamorphic Geology 22 (7), 671–687.

Walsh, E. O., Hacker, B. R., Gans, P. B., Grove, M., Gehrels, G., 2007. Protolith ages and exhumation histories of (ultra)high-pressure rocks across the Western Gneiss Region, Norway. Bulletin of the Geological Society of America 119 (3-4), 289–301.

Walte, N. P., Bons, P. D., Passchier, C. W., 2005. Deformation of melt-bearing systems - Insight from in situ grain-scale analogue experiments. Journal of Structural Geology 27 (9), 1666–1679.

Waters, D. J., 2001. The significance of prograde and retrograde quartz-bearing intergrowth microstructures in partially melted granulite-facies rocks. Lithos 56 (1), 97–110.

Wyllie, P. J., 1977. Crustal anatexis: An experimental review. Tectonophysics 43 (1-2), 41–71.

Yuguchi, T., Nishiyama, T., 2008. The mechanism of myrmekite formation deduced from steady-diffusion modeling based on petrography: Case study of the Okueyama granitic body, Kyushu, Japan. Lithos 106 (3-4), 237–260.

Table 1: Microprobe data of plagioclase (plag), K-feldspar (kfs), biotite (bte) and hornblende (hbl) compositions for migmatite sample WGR12 and shear zone sample WGR13[a].

	WGR12: Migmatite					**WGR13: Shear zone**				
Mineral	Qtz	Kfs	Plag	Bte	Hbl	Qtz	Kfs	Plag	Bte	Hbl
wt%	35%	33%	16%	14%	2%	46%	28%	17%	8%	1%
N		16	19	6	11		13	17	11	3
SiO_2	No analyses	64.242	61.001	36.310	39.275	No analyses	64.647	60.828	35.806	38.879
TiO_2		0.009	0.005	3.037	1.075		0.018	0.008	3.066	1.076
Al_2O_3		18.835	24.165	17.704	11.609		18.656	24.539	18.552	11.565
Cr_2O_3		0.006	0.005	0.025	0.015		0.007	0.009	0.031	0.016
FeO		0.049	0.114	19.243	21.173		0.034	0.104	19.096	20.949
MnO		0.003	0.008	0.506	0.827		0.008	0.007	0.297	0.834
MgO		0.005	0.007	8.619	7.105		0.004	0.006	8.993	7.012
CaO		0.051	5.987	0.018	11.484		0.058	6.177	0.033	11.452
BaO		0.699	0.015	0.090	0.008		0.671	0.024	0.144	0.000
Na_2O		0.973	8.310	0.075	1.455		1.014	8.074	0.052	1.460
K_2O		15.136	0.338	9.721	1.971		15.112	0.245	9.725	1.976
Total		100.009	99.955	95.348	95.997		100.228	100.021	95.794	95.218
No. of O		8	8	22	24		8	8	22	24
Si		2.974	2.740	5.539	6.640		2.984	2.729	5.432	6.630
Ti		0.000	0.000	0.348	0.137		0.001	0.000	0.350	0.138
Al		1.028	1.279	3.183	2.313		1.015	1.298	3.317	2.324
Cr		0.000	0.000	0.003	0.002		0.000	0.000	0.004	0.002
Fe		0.002	0.004	2.455	2.993		0.001	0.004	2.422	2.987
Mn		0.000	0.000	0.065	0.118		0.000	0.000	0.038	0.120
Mg		0.000	0.000	1.960	1.791		0.000	0.000	2.034	1.783
Ca		0.002	0.224	0.002	1.619		0.002	0.231	0.004	1.628
Ba		0.014	0.000	0.006	0.001		0.014	0.000	0.010	0.000
Na		0.087	0.724	0.022	0.477		0.091	0.702	0.015	0.483
K		0.894	0.019	1.892	0.425		0.890	0.014	1.882	0.430
Total		5.002	4.992	15.476	16.516		4.998	4.980	15.507	16.525

[a]Modal proportions for each mineral, including quartz (qtz) are shown by weight % (wt%). N is number of spot analyses per mineral, analyses were reject where totals are outside 99.0-101.0% for feldspars and below 95% for biotite and hornblende.

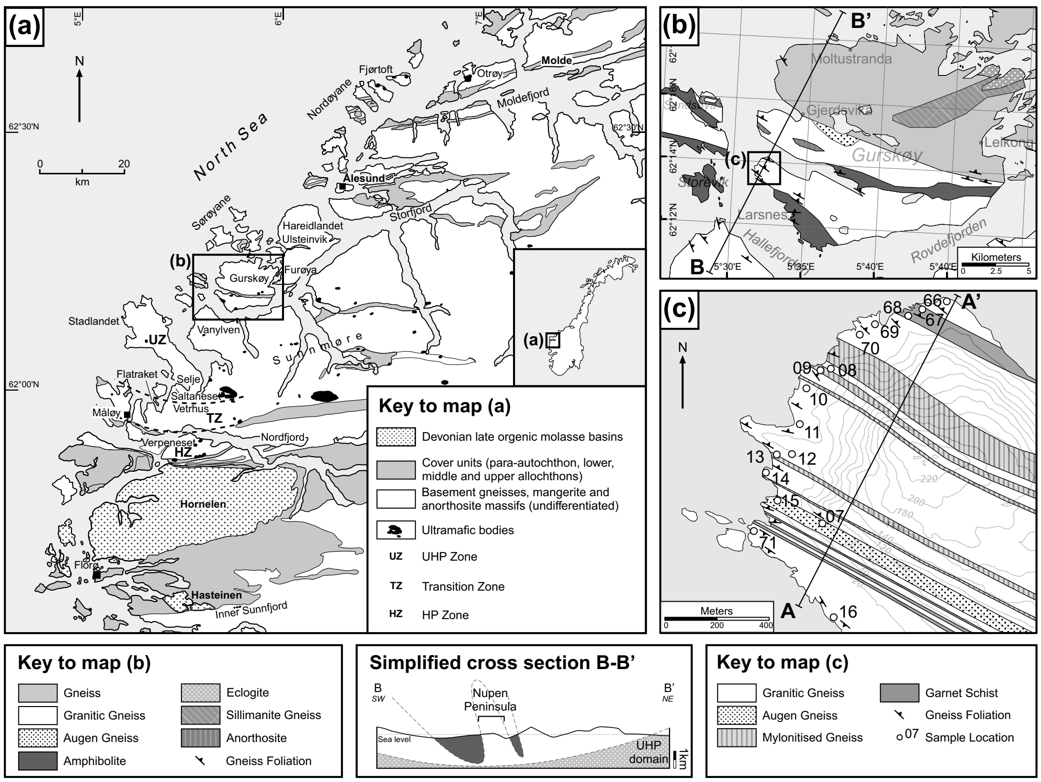

Figure 1: Geological map of (a) Western Gneiss Region with inset detail maps of (b) Gurskøy with section line B-B' and (c) Nupen Peninsula with sample locations and section line A-A' shown in Section 3.2 (Geological maps modified from Kildal, 1970; Lutro et al., 1997; Lutro and Tveten, 1998; Tveten et al., 1998; Carswell et al., 2003; Root et al., 2005).

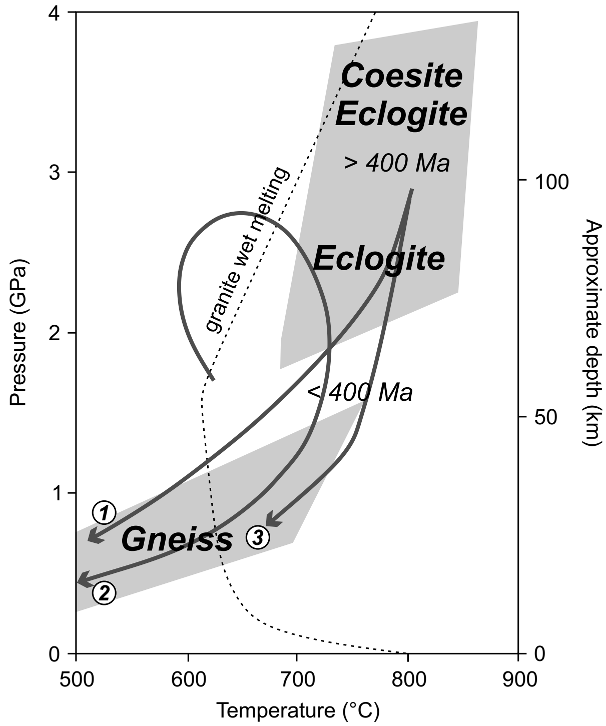

Figure 2: P-T diagram showing the relationship of WGR metamorphic conditions recorded by eclogite and gneiss in the Nordfjord-Stadlandet and Sørøyane UHP domains and surrounding HP domains. P-T paths from 1) Gordon et al. (2016), 2) Labrousse et al. (2002) and 3) Gordon et al. (2013), granite solidus from Auzanneau et al. (2006). Timing of peak UHP and HP metamorphism from Hacker et al. (2010). Note that although both eclogite and gneiss likely experienced UHP conditions, the gneiss equilibrated at much lower PT conditions during decompression.

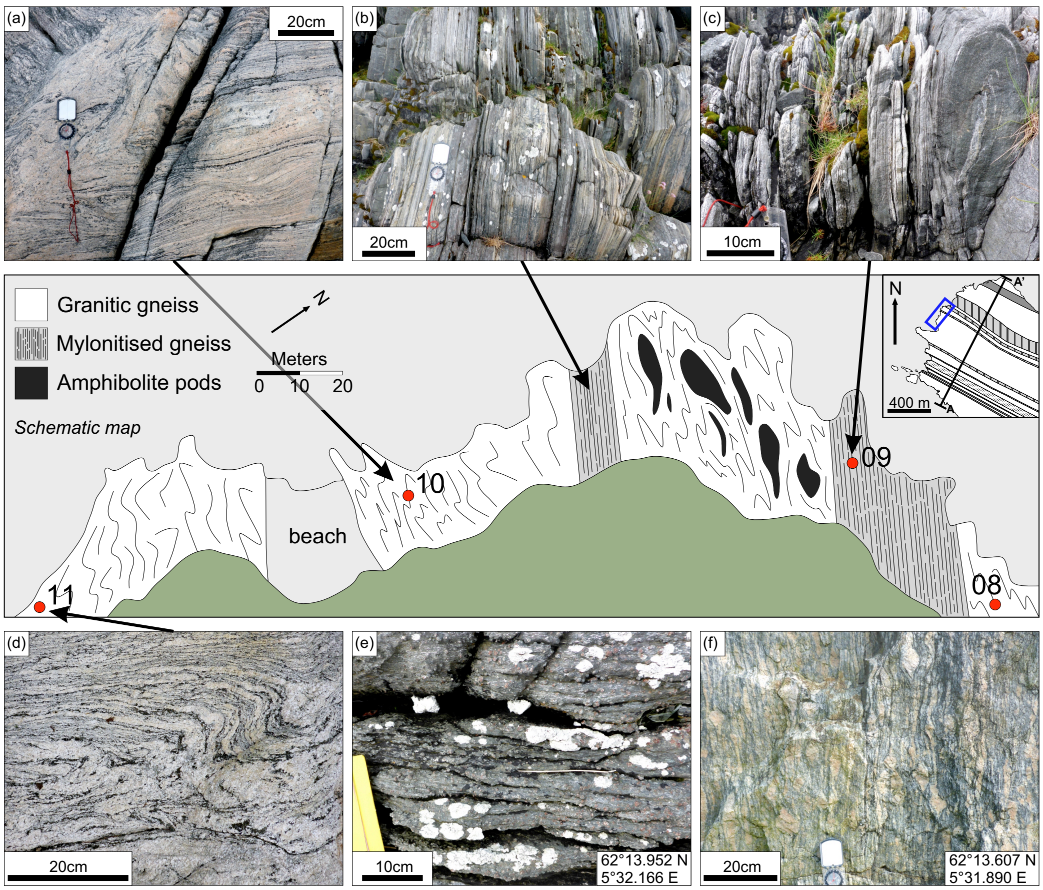

Figure 3: Detailed geological field map showing variation of the gneiss at Nupen, foliation pattern and amphibolite pod location is representative. Photos (a-f) are characteristic outcrop photos of the (a,d) migmatized gneiss and (b,c) mylonitized gneiss and not shown on detailed field map (e) garnet schist and (f) augen gneiss.

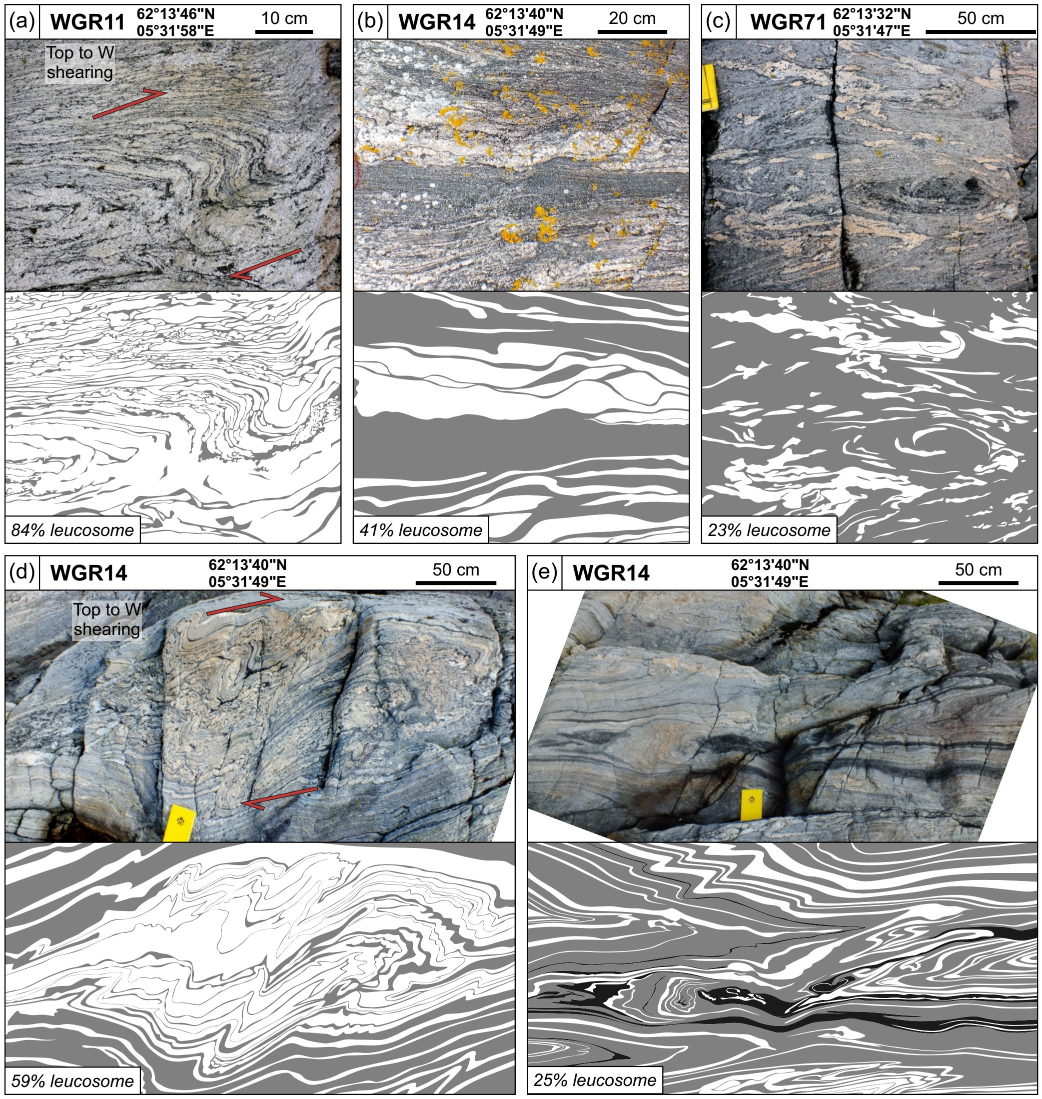

Figure 4: Field photographs with schematic drawings to emphasise the leucosome and melanosome segregation at outcrop scale. Examples shown from the WGR; (a) Leucosome-rich outcrop with top to the west shearing; (b) Ophthalmic layers in leucosome; (c) Surreitic/dilational migmatite; (d) Folded stromatic migmatite with top to the west shearing; (e) Folded stromatic migmatite with leucosome, mesosome and melanosome. Migmatite nomenclature after Ashworth (1985).

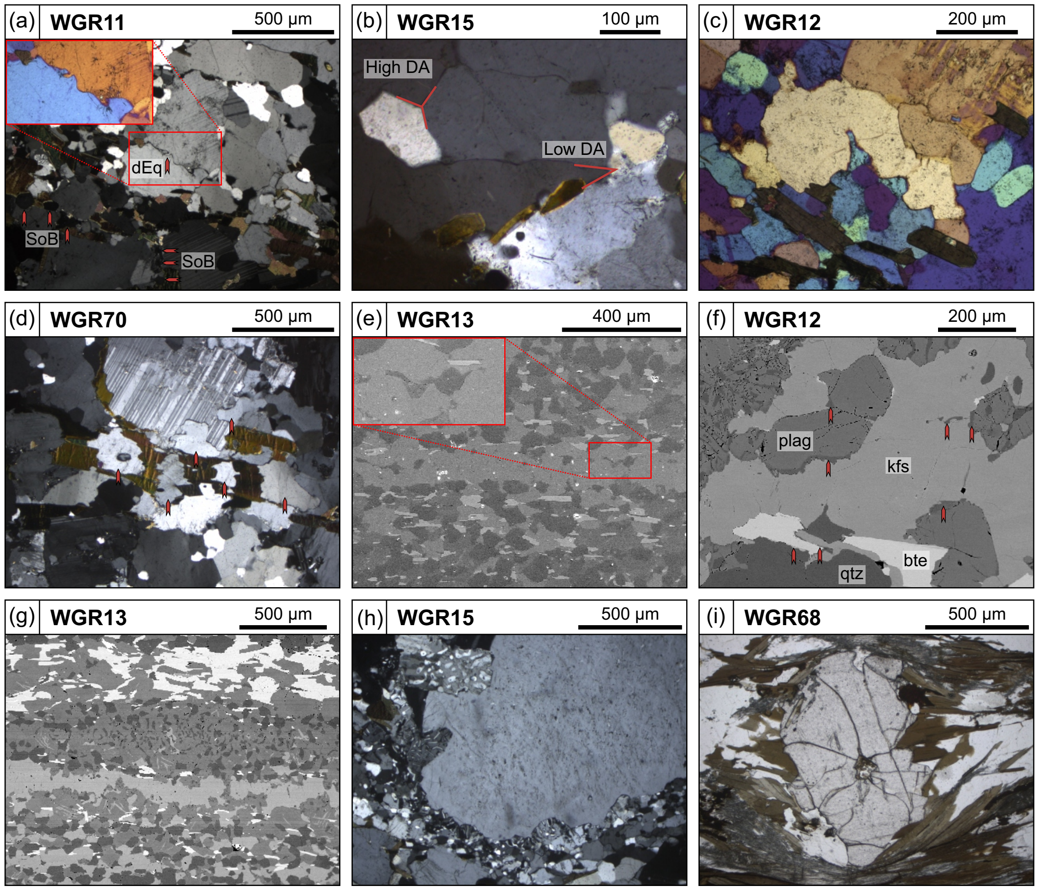

Figure 5: Melt microstructures in migmatitic gneiss from photomicrographs in plain-polarised light (i), cross-polarised light (a, b, d, h), cross-polarised light and gypsum plate (a-inset, c) and SEM-BSE image (e, f, g). (a) Migmatite with plagioclase and quartz grain boundaries in disequilibrium (dEq), string of beads texture (SoB) in quartz along plagioclase grain boundaries indicated by arrows. (b) Augen gneiss with high and low dihedral angles (DA) between quartz grains. (c-d) Migmatite with interstitial quartz melt infilling pore space. (e) Shear zone sample with interstitial quartz melt infilling pore space. (f) Migmatite with quartz (qtz) films along grain boundaries of plagioclase (plag), K-feldspar (kfs) and biotite (bte). (g) Shear zone sample with myrmekite and disequilibrium grain boundaries. (h) Augen gneiss with quartz-plagioclase myrmekite surrounding large K-feldspar grain. (i) Garnet schist with peritectic garnet surrounded by sillimanite, biotite and quartz.

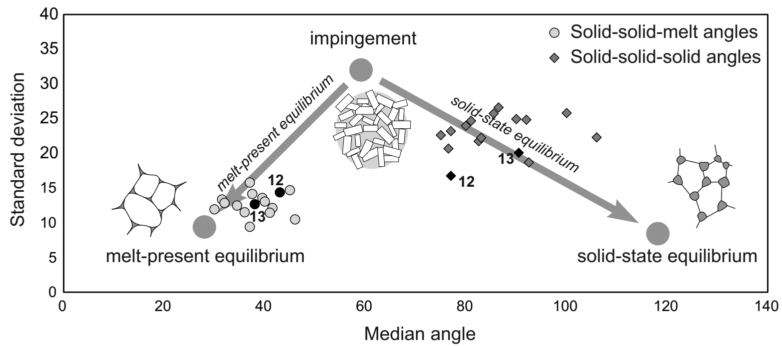

Figure 6: Dihedral angles from the WGR samples for solid-solid-melt boundaries (○) and solid-solid-solid boundaries (◇). Results for samples WGR12 (migmatite) and WGR13 (shear zone) are identified and shown with filled in black symbols. Also shown is a schematic diagram showing end-member solid-solid-melt dihedral angle populations (Adapted from Holness et al., 2005).

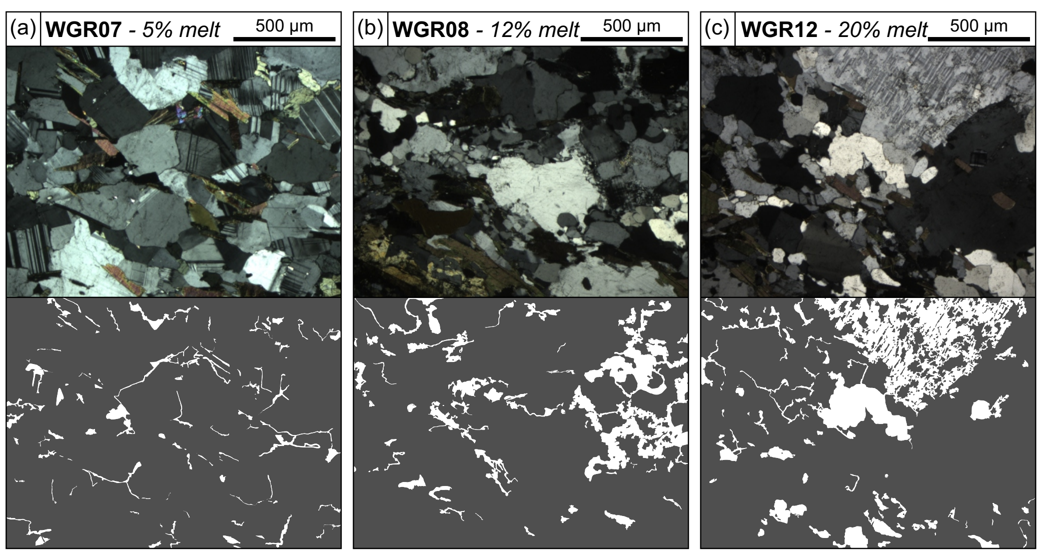

Figure 7: Top: Photomicrographs of melt on grain boundaries in SIP migmatites in plane polarised light. Bottom: Melt (white) vs. solid (grey) image analysis interpretations of each photomicrograph.

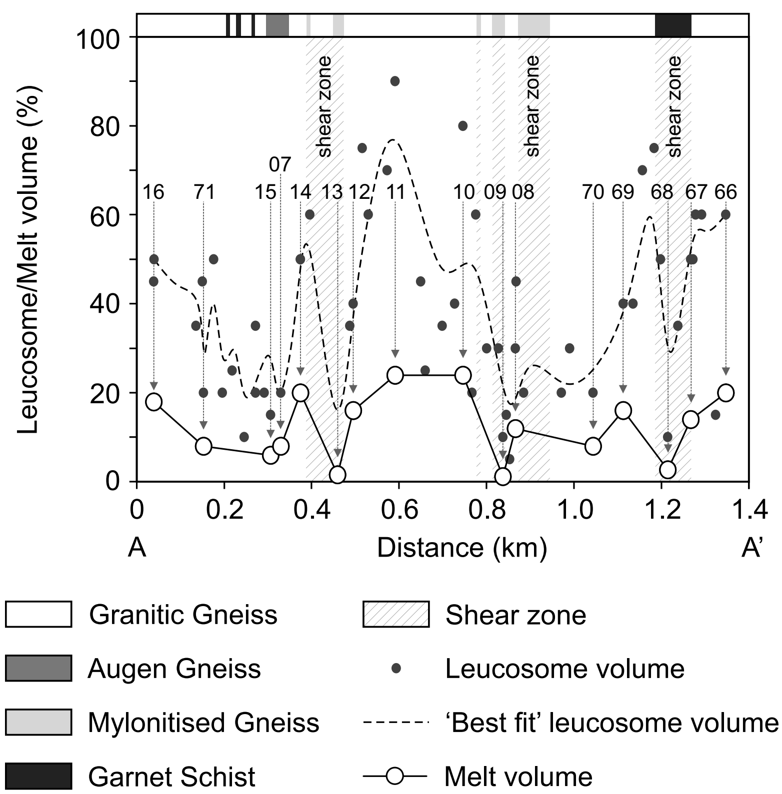

Figure 8: Leucosome and melt volume over the Nupen Peninsula (Figure 1 Map C, section A-A'). Macroscale leucosome volume calculated in the field and via image analysis at the outcrop scale and microscale melt volume calculated from image analysis of thin sections and SEM images.

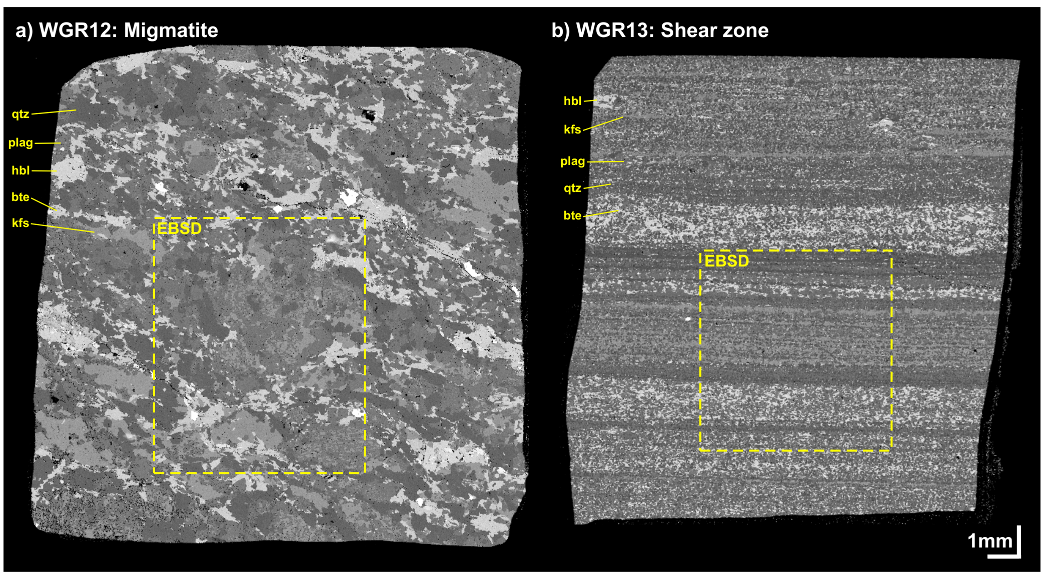

Figure 9: Backscattered electron maps of (a) migmatite sample WGR12 and (b) shear zone sample WGR13. Maps are at the same scale with 1 mm bar shown for scale. Dashed yellow boxes indicate area of EBSD analysis.

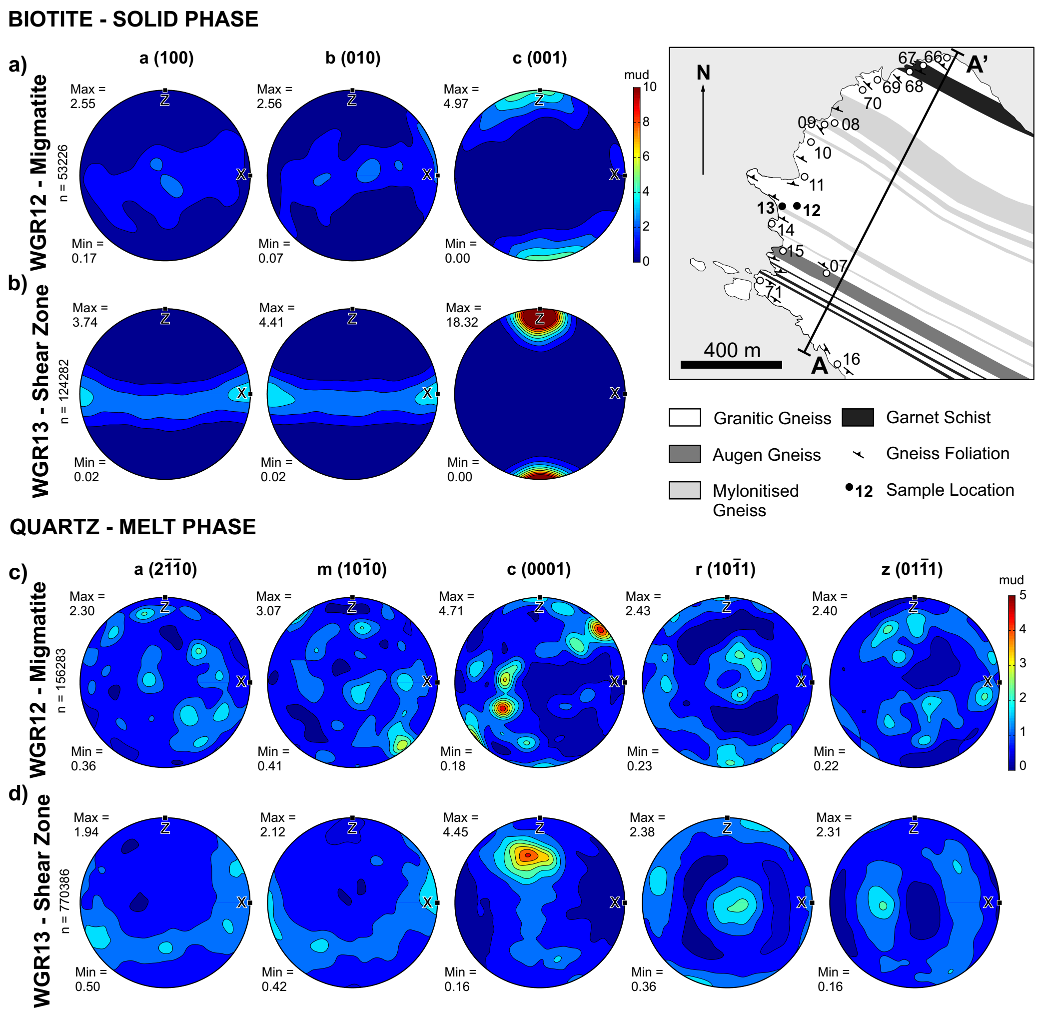

Figure 10: EBSD-derived CPO of biotite (a, b) and quartz (c, d) in kinematic coordinate system for migmatized gneiss sample WGR12 (a, c) and mylonitized gneiss sample WGR13 (b, d). All stereographic projections are lower hemisphere and CPO are contoured in terms of multiples of the uniform distribution (mud). Inset map shows locations of adjacent mylonitized and migmatized gneiss samples.

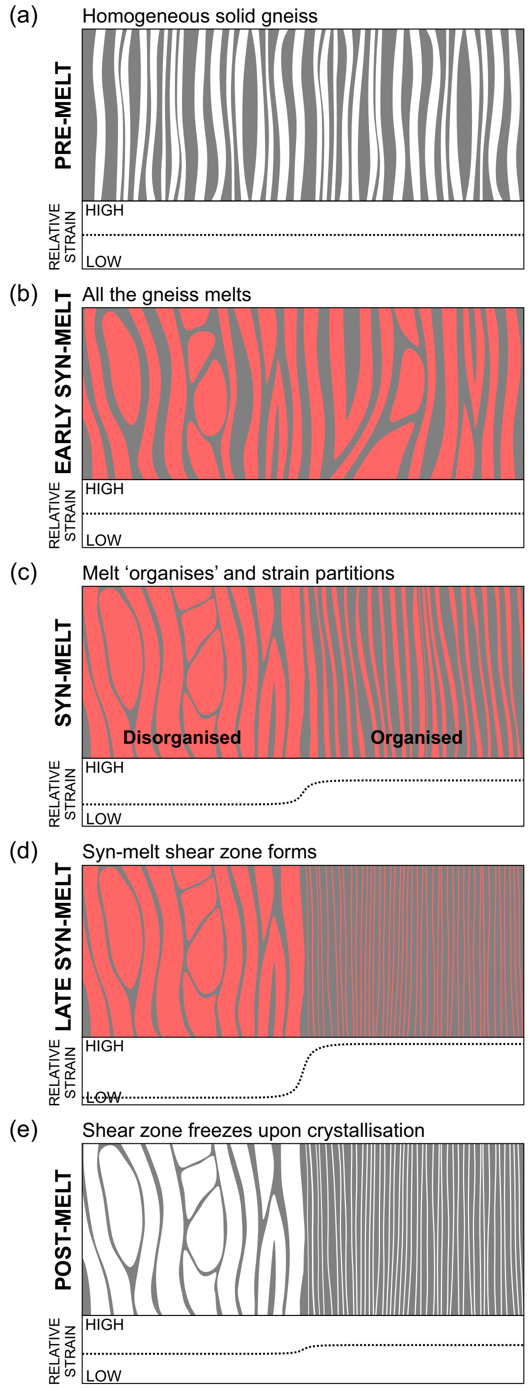

Figure 11: Schematic diagrams to show how strain localisation can vary during syn-melt shearing of a migmatized gneiss. Under each stage of the models are relative strain profiles indicating areas of strain localisation. (a) Homogeneous solid gneiss where strain is distributed evenly; (b) melting is pervasive throughout the leucosome; (c) melt organises into layers whereas elsewhere it remains as disorganised 'pools'; (d) runaway organisation effect produces syn-melt shear zones; (e) structure freezes upon crystallisation giving a mylonite-like outcrop style in the field.